SUPPORTING INFORMATION

Mechanism Insights into The Role of Support Mineralization Layer toward Ultrathin Polyamide Nanofilm for Ultrafast Molecular Separation

Qiangqiang Song,[a,b] Yuqing Lin,* [c] Takafumi Ueda,[a] Titik Istirokhatun,[a,b] Qin Shen,[a,b] Kecheng Guan,[a] Tomohisa Yoshioka,[a] and Hideto Matsuyama* [a,b]

[a] Research Center for Membrane and Film Technology, Kobe University, Kobe 657-8501, Japan.

[b] Department of Chemical Science and Engineering, Kobe University, Kobe 657-8501, Japan.

[c] School of Resources and Envionmental Engineering, East China University of Science and Technology, Shanghai, 200237, China

To whom all correspondence should be addressed.

Email: linyuqing@ecust.edu.cn; matuyama@kobe-u.ac.jp;

Table of Contents

Results and Discussion

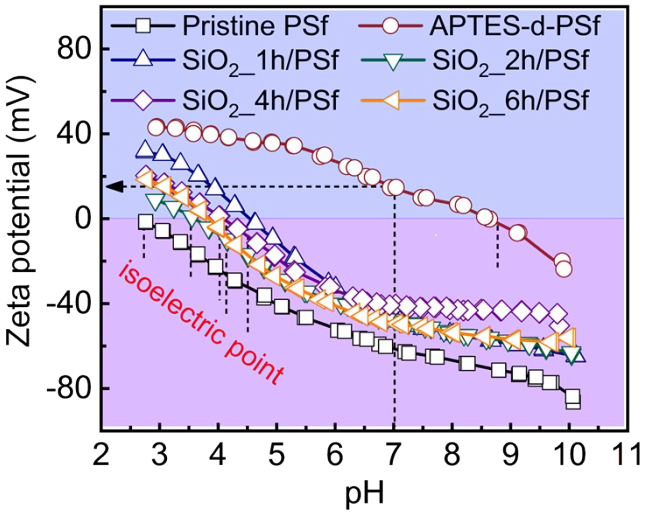

Fig. S1 Surface zeta potential of pristine PSf, APTES-d-PSf, and SiO_2/PSf ultrafiltration membranes.

The membrane surface zeta potentials were estimated by measuring the zeta potentials in a background electrolyte solution of 1 mM KCl. As shown in **Fig. S1**, the virgin PSf is negatively charged (-62.55 mV) at neutral condition (pH=7) with an isoelectric point (IEP) of 2.72. The APTES-d-PSf is positively charged with a surface potential of 18.69 mV (pH=7) and IEP of 8.77 ascribing to the deposited positive APTES polyelectrolyte layer after the poly-condensation process.[1-3] And the SiO_2/PSf membranes are negatively charged with silicification durations goes on. Taking SiO_2_2h/PSf membrane as an example, a negative surface (IEP: 3.52) with -47.48 mV surface potential at a neutral condition (pH value of 7) could be obtained

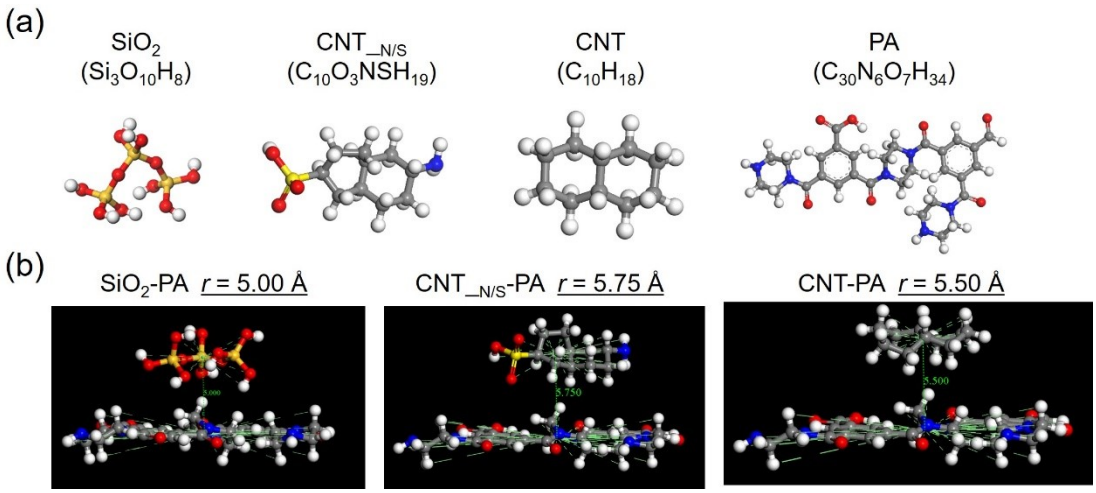

Fig. S2 (a) The chemical structures of SiO_2, $CNT\_{N/S}$, CNT, and PA; (b) snapshots of SiO_2-PA, $CNT\_{N/S}$-PA, and CNT-PA at the lowest interaction energy positions.

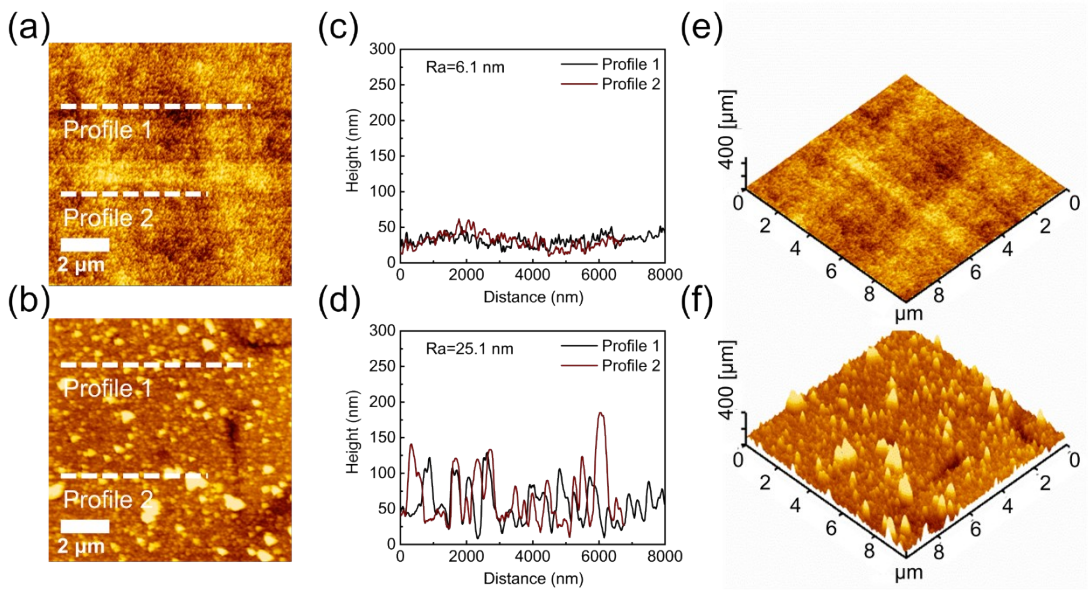

Fig. S3 AFM topographic images (left-hand panel), height profile (middle panel), and AFM surface 3D morphology images (right-hand panel) of pristine PSf (a, c, e) and SiO_2_4h/PSf (b, d, f) ultrafiltration membranes.

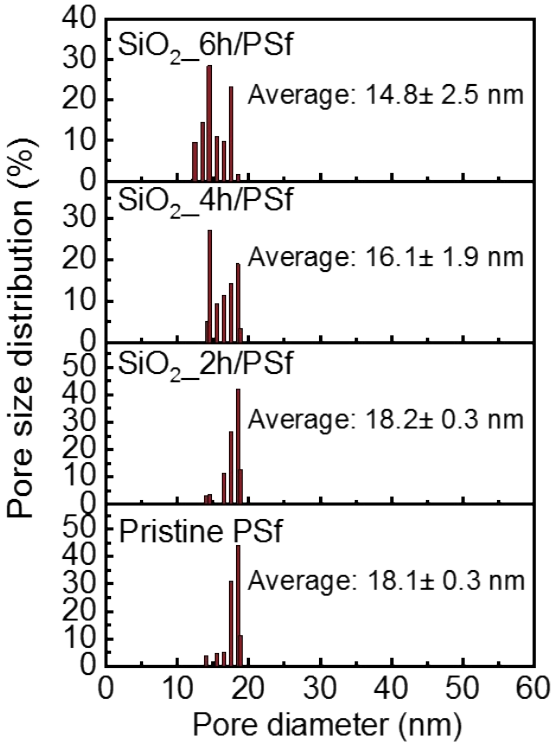

Fig. S4 Pore size and pore size distribution of pristine PSf and SiO_2/PSf membrane substrates.

The pore size of PSf membranes tends to decrease because of the larger SiO_2 nucleus inside/surficial deposition accompanied by the possible pore blocking effect with prolonged silicification durations.

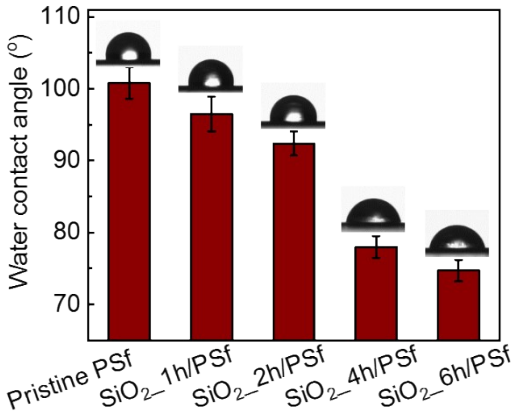

Fig. S5 Surface wettability of pristine PSf and various SiO_2/PSf membranes.

The water contact angles of the PSf-based supporting membranes were 100.8°, 96.5°, 92.4°, 78.1°, and 74.9° for pristine PSf, SiO_2_1h/PSf, SiO_2_2h/PSf, SiO_2_4h/PSf, and SiO_2_6h/PSf membranes, respectively. This indicates that the wettability of the substrate surface could be controlled by changing the mineralization duration.

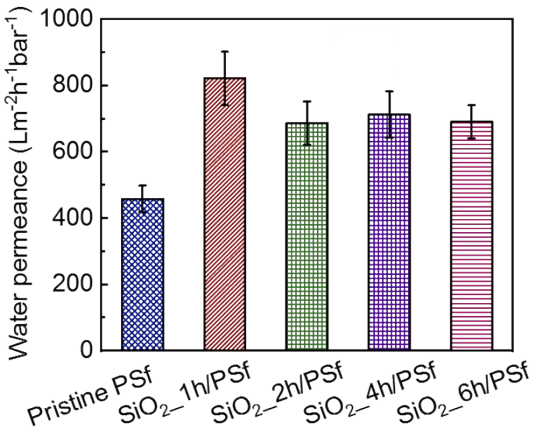

Fig. S6 Pure water permeance of pristine PSf and SiO_2/PSf supports.

The filtration tests were performed in a crossflow system with an effective test area of 8.05×10^{-4} m^2. The water flux ($L \cdot m^{-2} \cdot h^{-1} \cdot bar^{-1}$) of the porous PSf substrates was determined from the variations in the weight of the permeate for a specified time after the permeance reached a steady state. The applied trans-membrane pressure is 0.5 bar with a relatively low circulation flow rate of 0.01 $L \cdot min^{-1}$. It was calculated based on Equation (3). The water fluxes before and after the silicification treatment process were 458 $L \cdot m^{-2} \cdot h^{-1} \cdot bar^{-1}$, 821 $L \cdot m^{-2} \cdot h^{-1} \cdot bar^{-1}$, 686 $L \cdot m^{-2} \cdot h^{-1} \cdot bar^{-1}$, 712 $L \cdot m^{-2} \cdot h^{-1} \cdot bar^{-1}$, and 690 $L \cdot m^{-2} \cdot h^{-1} \cdot bar^{-1}$ for pristine PSf, SiO_2_1h/PSf, SiO_2_2h/PSf, SiO_2_4h/PSf, and SiO_2_6h/PSf, respectively. The changes in the pure water permeance can be attributed to the greatly enhanced water affinity (hydrophilicity). It is noted that a denser and thicker mineralization interlayer will have an adverse influence on water permeance, manifested by the slightly decreased water permeance with the excess silicification duration.[1, 2] The water permeance was obtained by calculating the average of 3-time measurement results for three samples prepared from different batches.

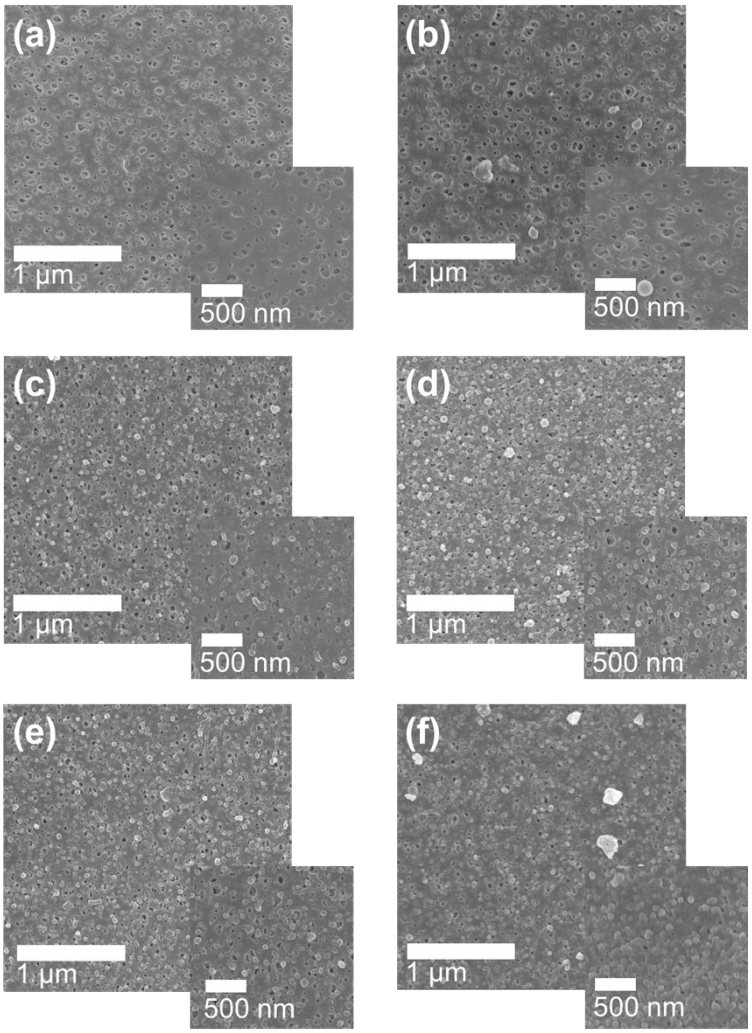

Fig. S7 FESEM images of (a) pristine PSf, (b) SiO_2_4h_PSf without APTES pre-treatment, (c) SiO_2_1h/PSf, (d) SiO_2_2h/PSf, (e) SiO_2_4h/PSf, and (f) SiO_2_6h/PSf porous supports.

As shown in **Fig. S7**, with the modification of SiO_2 mineralization, the PSf surface was gradually covered by ultrafine SiO_2 nanoparticles (50–100 nm) with a more curved and roughened surface structure. This intriguing and unique structure is more conducive to the formation of defect-free ultrathin crumpled nanofilms with a greater number of nano-voids for easier transport of water molecules. However, a continuous

mineralization layer could be formed without the APTES pre-treatment process, confirming the critical role of APTES for ultrafine silicification layer formation.[3]

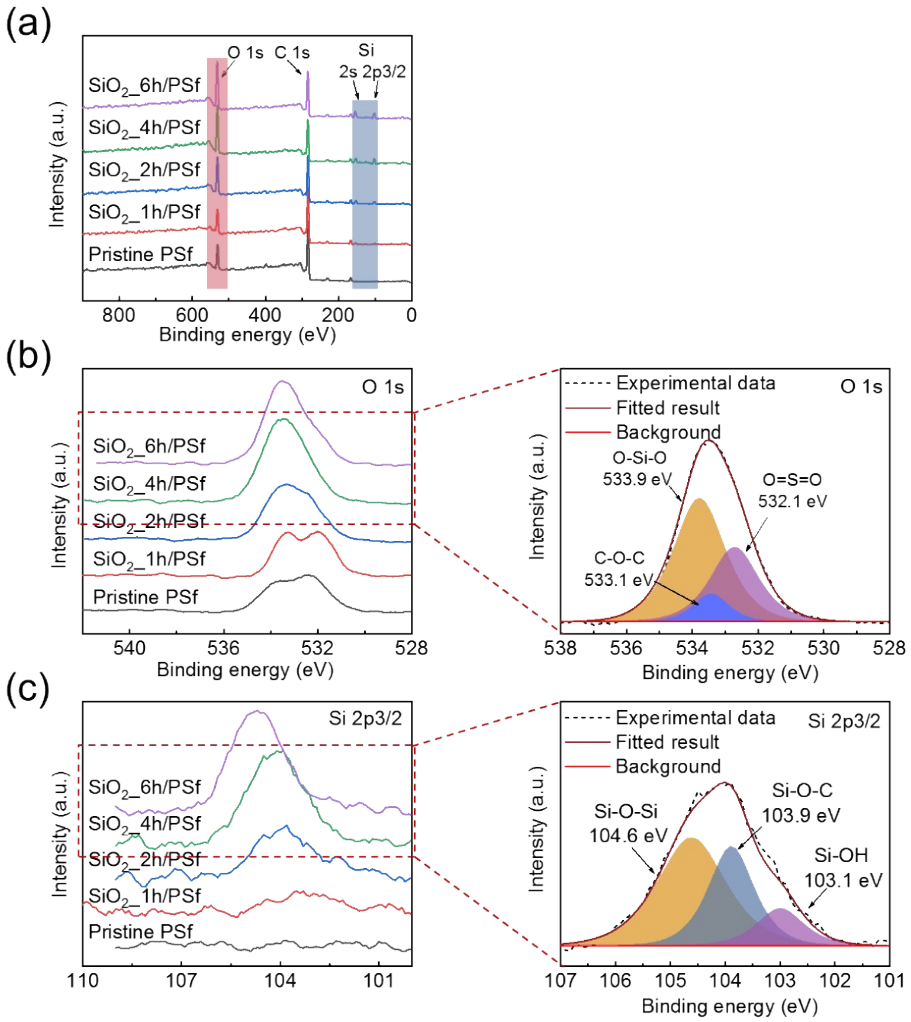

Fig. S8 XPS characterization of (a) wide scan and core-level narrow scan of (b) O 1s and (c) Si 2p3/2 elements of pristine PSf and SiO_2/PSf ultrafiltration membranes.

As shown in **Fig. S8**, the full-scan XPS spectra (a) of the SiO_2/PSf membranes display more intense O and Si peaks than that of the pristine PSf support because of the significantly enhanced (b) O-Si-O (533.9 eV), C-O-C (533.1 eV), (c) Si-O-Si (104.6 eV), and Si-OH (103.1 eV) in the high-resolution narrow scan spectra of O 1s and Si 2p3/2. These results confirm that the surface chemical composition changes with increasing mineralization duration. Notably, the appearance of Si-OH (103.1 eV) originates from the APTES monomer on the PSf support.[4]

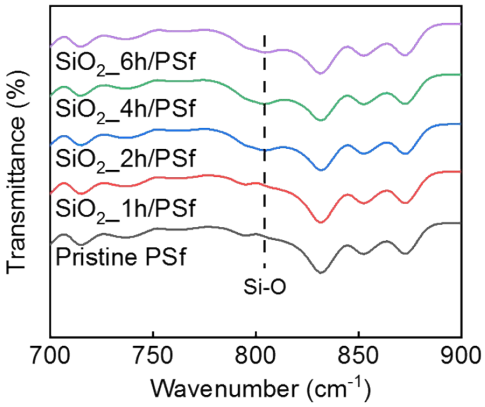

Fig. S9 FTIR characterization of pristine PSf, SiO_2_1h/PSf, SiO_2_2h/PSf, SiO_2_4h/PSf, and SiO_2_6h/PSf membranes.

According to the FTIR spectrum, all porous PSf membranes exhibited almost similar absorption curves, except for the gradually increased absorption peak at 802 cm^{-1} with prolonged silicification time, which is ascribed to the symmetrical stretching vibration of the Si-O bond. This result indicates that the SiO_2 nanoparticles could be deposited on the PSf substrates via an electrostatically induced self-assembled strategy.

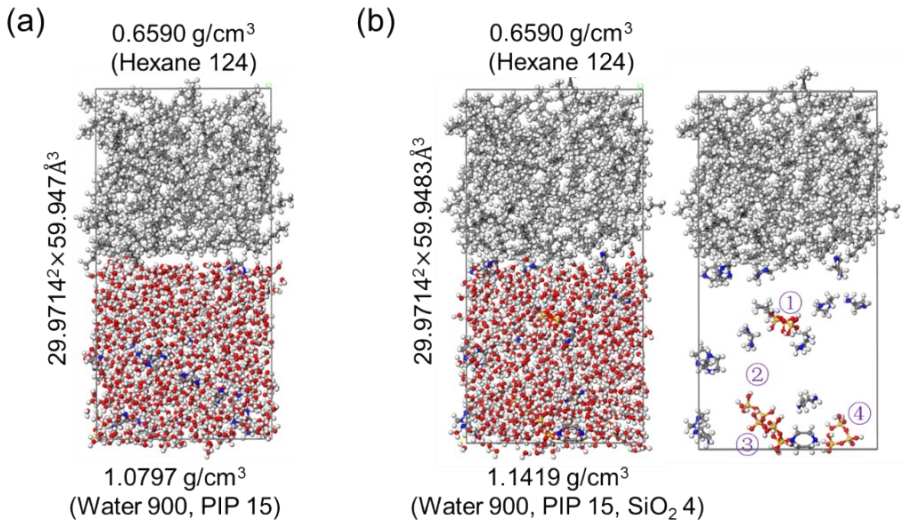

Fig. S10 Profiles of MD simulation of (a) n-hexane-water system and (b) n-hexane-water (hide)-SiO_2 system.

A simulation cell with a size of 29.9714 Å × 29.9714 Å × 59.9470 Å and periodic boundaries in all directions was prepared. In the hexane-water system, 15 PIP and 900 water molecules were included to model an aqueous phase with a density of 1.0797 $g \cdot cm^{-3}$, and 124 n-hexane molecules were included to model a hexane phase with a density of 0.6590 $g \cdot cm^{-3}$, as shown in **Fig. S10 (a)** In the hexane-water-SiO_2 system, four SiO_2 molecules were distributed in the aqueous cell of the hexane-water system, as shown in **Fig. S10 (b)**. Besides, the center coordinate of four SiO_2 particles inside the n-hexane-water-SiO_2 system are as follows: ☙ (6.09605, 15.6308, 21.2589), & (20.5660, 20.3620, 5.80330), ● (5.88577, 16.6026, 2.13580), and ❍ (29.5996, 6.26715, 2.27770).

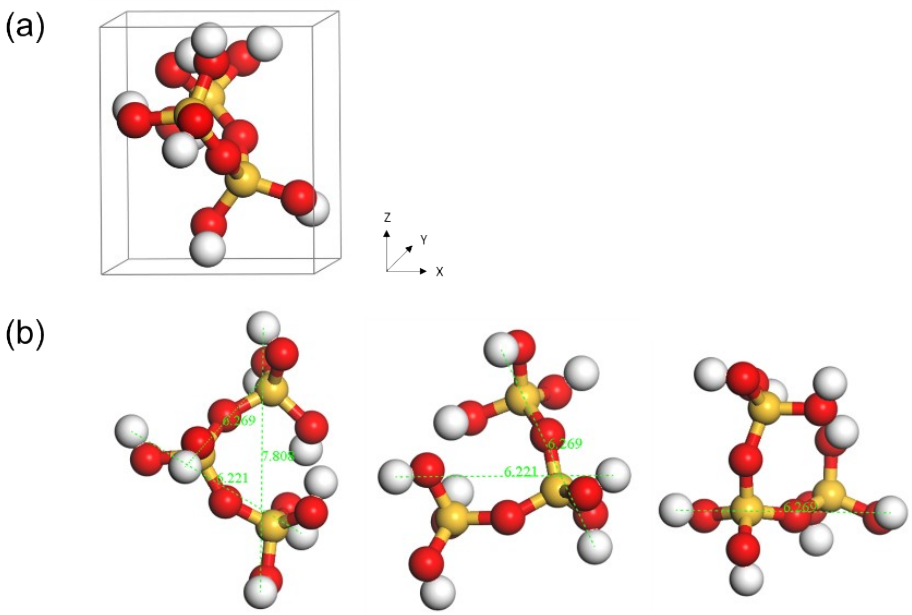

Fig. S11. (a) The size and volume of SiO_2 nanoparticles were calculated by locating them inside a rectangular parallelepiped (with the outer surface of the cuboid tangent to the outermost atoms of SiO_2); (b) interatomic distance between the centers of atoms (the radius of atom ball size is 0.5 Å).

The volume of SiO_2 particles employed in this calculation was approximately 5.9 Å × 8.8 Å × 6.8 Å (calculated based on the size of the rectangular parallelepiped).

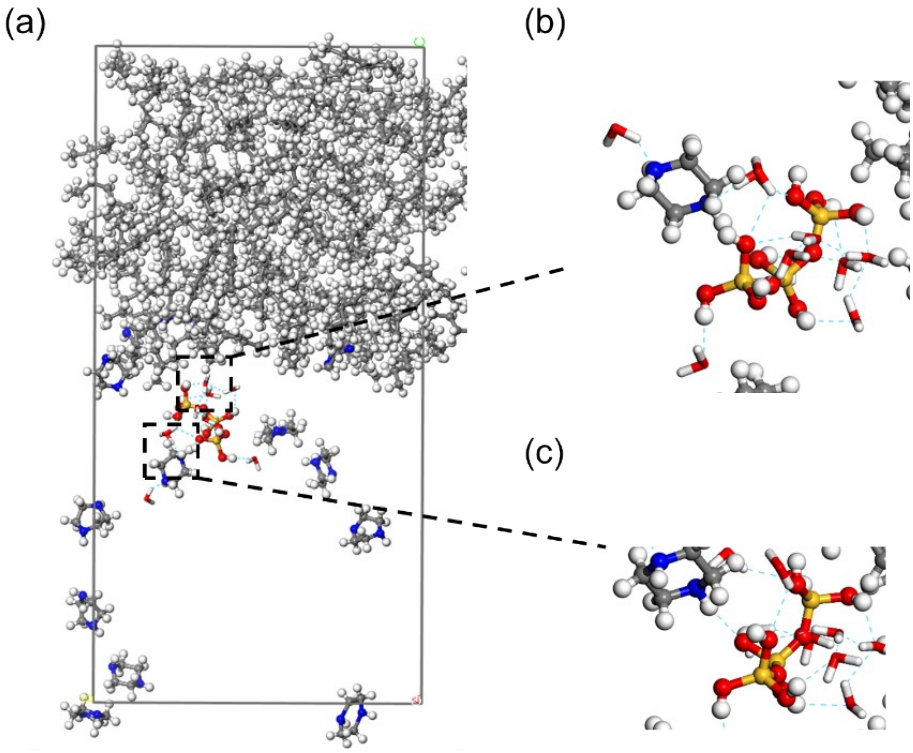

Fig. S12 (a) Pictures of the n-hexane-water (hide) interface in the presence of SiO_2 particles; chemical interactions of SiO_2 particles with (b) water molecules and (c) PIP molecules via hydrogen bonding.

The SiO_2 particle ($Si_3O_{10}H_8$) with a molecular weight (Mw) of 252.3 $g \cdot mol^{-1}$ was terminated with eight hydrogen atoms. Eight hydroxyl functional groups are located at the molecular edge and can form hydrogen bonds with water and PIP molecules.

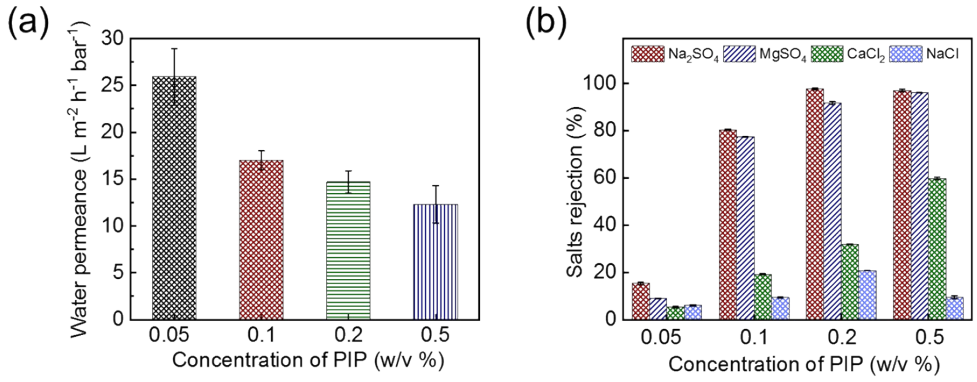

Fig. S13 (a) Pure water permeance and (b) inorganic salt rejection ratio of PA_SiO_2_4h/PSf TFC membrane fabricated at various PIP concentrations and the same TMC concentration of 0.1% (w/v) with a reaction duration of 30 s.

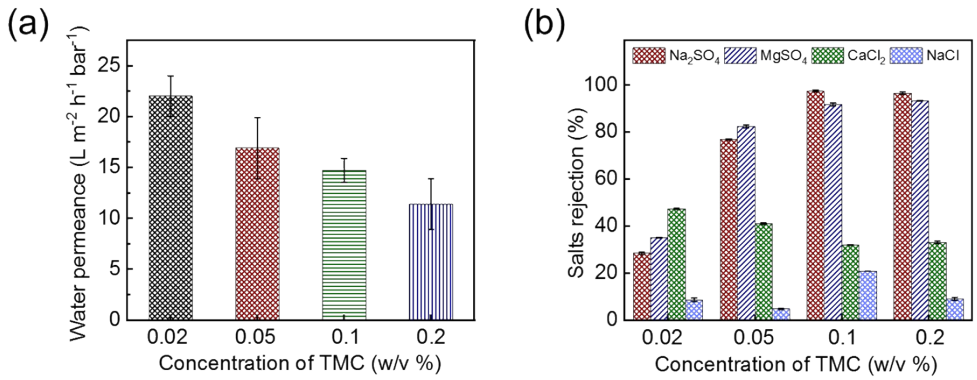

Fig. S14 (a) Pure water permeance and (b) inorganic salt rejection ratio of PA_SiO_2_4h/PSf TFC membranes fabricated at various TMC concentrations and the same PIP concentration of 0.2% (w/v) with a reaction duration of 30 s.

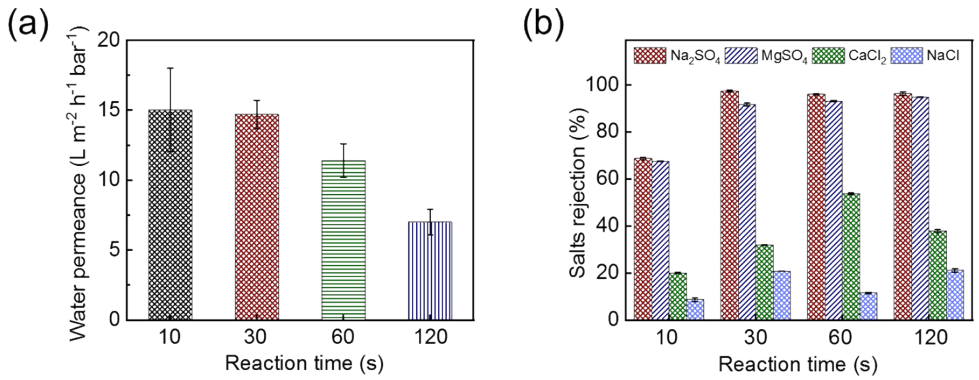

Fig. S15 (a) Pure water permeance and (b) inorganic salt rejection ratio of PA_SiO_2_4h/PSf TFC membranes fabricated at various reaction durations. All membranes were formed with the same PIP (0.2% (w/v)) and TMC (0.1% (w/v)) concentrations.

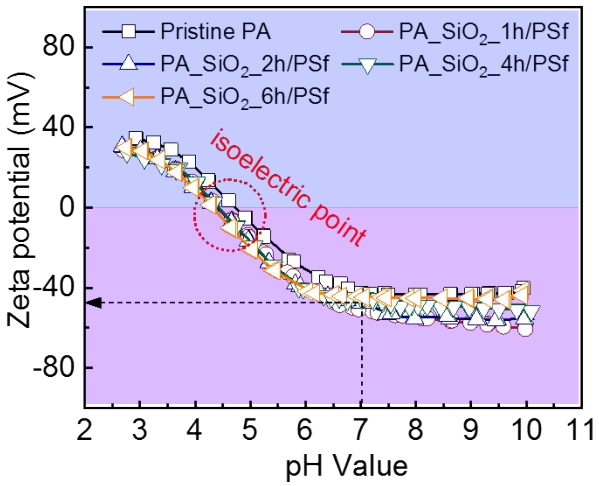

Fig. S16 Surface potential of pristine PA and PA_SiO_2/PSf TFC membranes. All the measurements were performed at 398 K and repeated four times.

The membrane surface zeta potentials were estimated by measuring the zeta potentials in a background electrolyte solution of 1 mM KCl. According to the measured zeta potential data of the pristine PA and PA_SiO_2/PSf TFC membranes, all membranes exhibited typical negatively charged outermost PA surfaces in neutral environments because of the hydrolysis of acyl chloride.[5] The isoelectric point (IEP) value estimated from the above analysis was approximately 4.6. The related zeta potential value at pH = 7 was -49.4 mV.

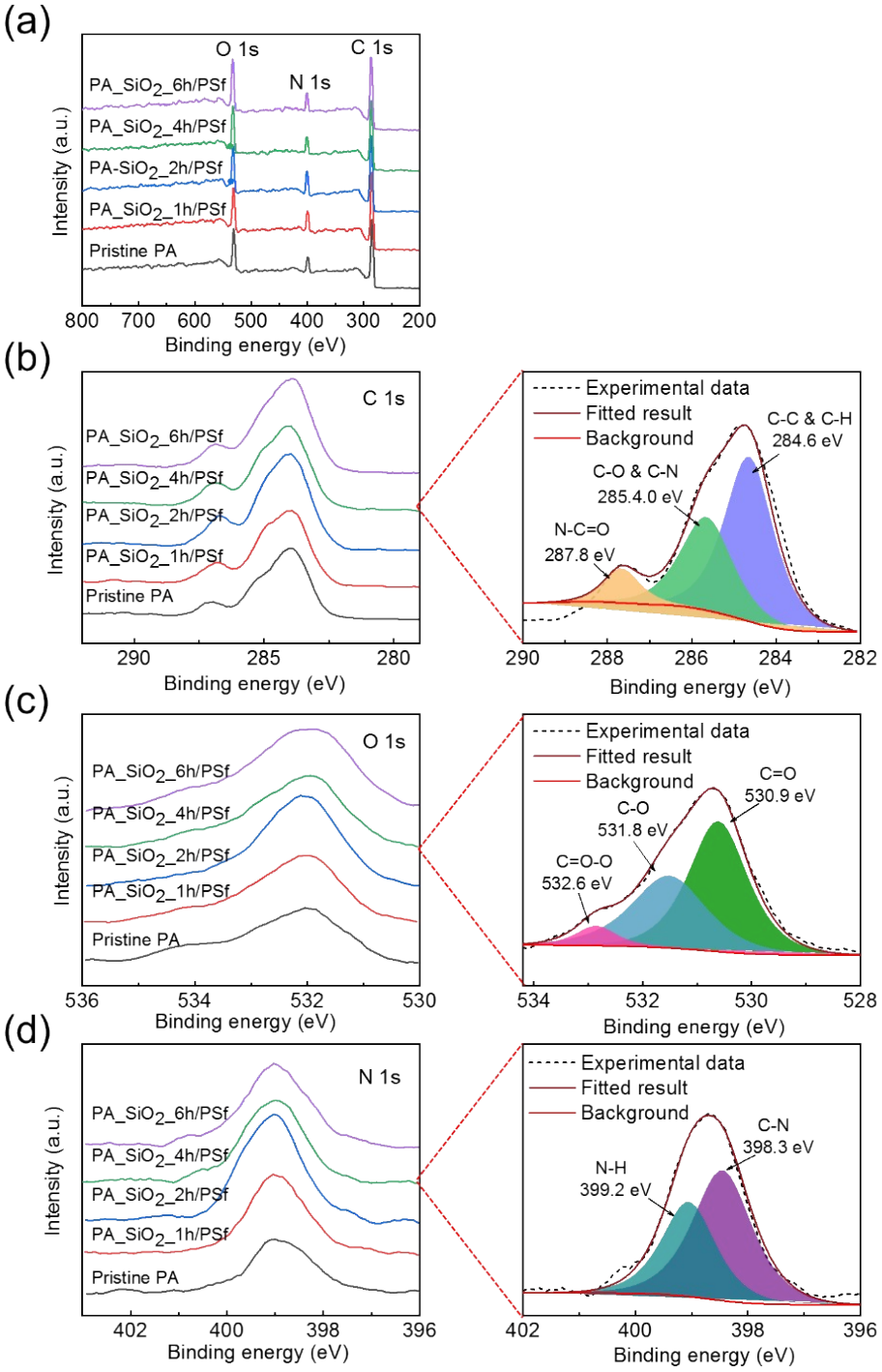

Fig. S17 (a) XPS characterizations of (a) wide scan and core-level narrow scan of (b) C 1s, (c) O 1s, and (d) N 1s elements of pristine PA and PA_SiO_2/PSf TFC membranes.

The deconvoluted scan spectra of the PA-based TFC membranes exhibit typical peaks corresponding to N-C=O (287.8 eV), C-O and C-N (285.4 eV), C-C, and C-H (284.6 eV) for C 1s; C=O-O (532.6 eV), C-O (531.8 eV), and C=O (530.9 eV) for O 1s; N-H (399.2 eV) and C-N (398.3 eV) for N 1s. These peaks confirm the chemical composition of typical PA films fabricated by interfacial polymerization.[6]

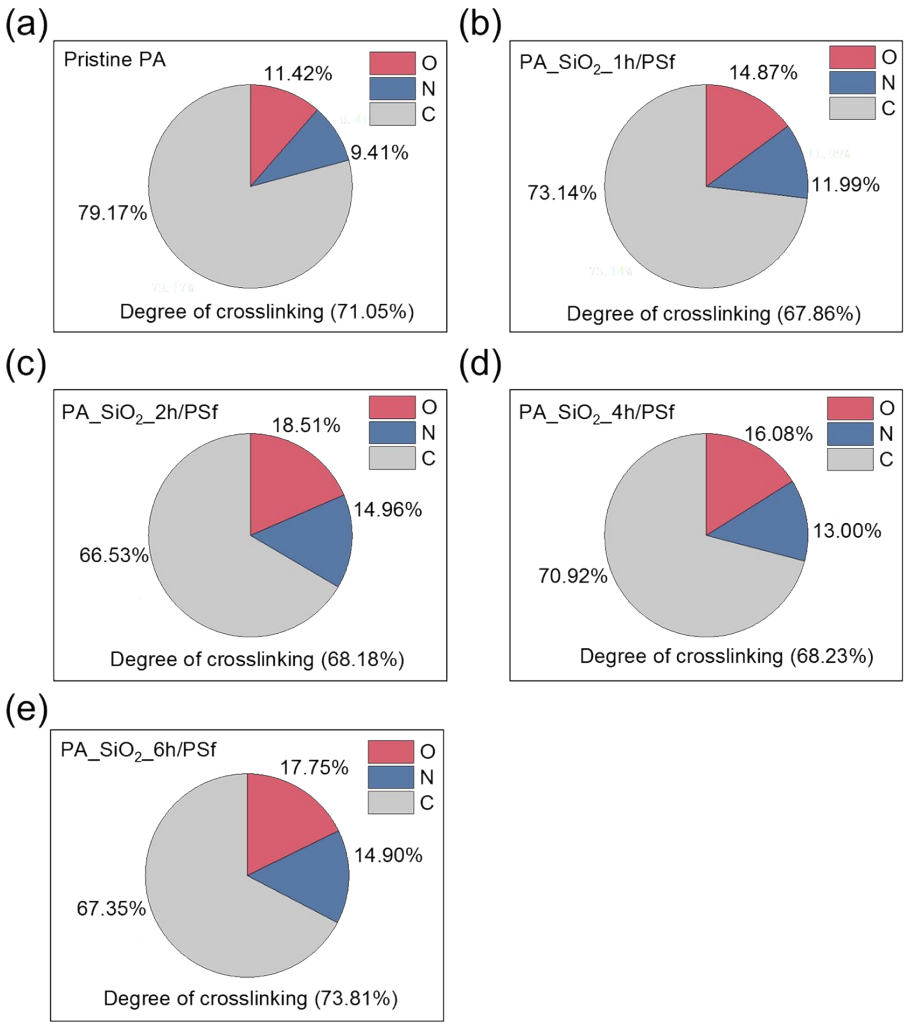

Fig. S18 Crosslinking degree of pristine PA and PA_SiO_2/PSf TFC membranes.

From the above results and **Fig. S18**, the PA-based TFC membrane exhibited a higher degree of crosslinking (~70%). However, the SiO_2/PSf PA nanofilms with longer mineralization times (4 h and 6 h) exhibited a slightly compromised rejection ratio for divalent anions. This was because of the relatively loose-selective-PA nanofilm with enlarged pore size and free volume originating from the acyl chloride of TMC when in contact with the moistened SiO_2/PSf supports.[7]

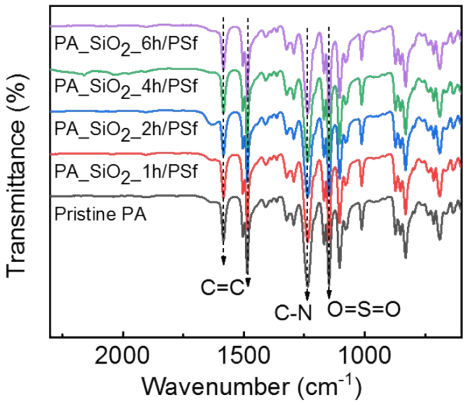

Fig. S19 ATR-FTIR spectra of pristine PA and PA_SiO_2/PSf TFC membranes.

According to the FTIR spectra of pristine PA and PA_SiO_2/PSf TFC membranes, all PA membranes exhibited similar infrared absorption characteristic peaks. Specifically, the peaks located at 1580 cm^{-1} and 1483 cm^{-1} were attributed to the C=C bond in-plane aromatic PA, and the peak located at 1239 cm^{-1} was attributed to C-N stretching, confirming the presence of the PA nanofilm on the PSf substrate.[8]

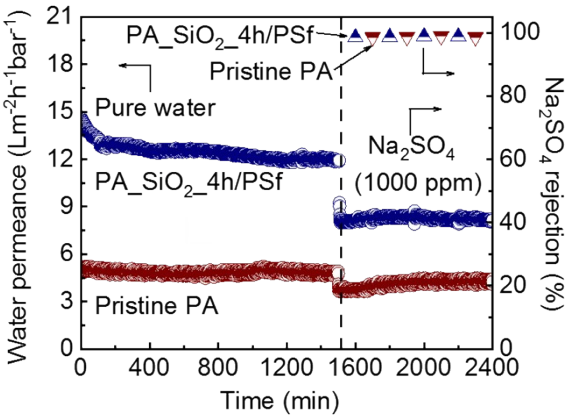

Fig. S20 Long-term filtration of pristine PA and PA_SiO_2/PSf TFC membranes for pure water and 1000 ppm Na_2SO_4 aqueous solution under 10 bar and 398 K for 2400 min.

The pure water permeance of the membrane decreased at the initial stage of the filtration experiment because of the well-known compaction effect. The water flux decreased from 15.2 to 14.5 $L \cdot m^{-2} \cdot h^{-1} \cdot bar^{-1}$ during the first 30 min of the filtration test. After 1600 min long-term pure water filtration, the PA_SiO_2_4h/PSf membrane still has acceptable water permeance of 12.3 $L \cdot m^{-2} \cdot h^{-1} \cdot bar^{-1}$ and high rejection (99.0%) toward Na_2SO_4. In addition, the PA_SiO_2_4h/PSf TFC membrane showed structural robustness similar to that of the pristine PA membrane.

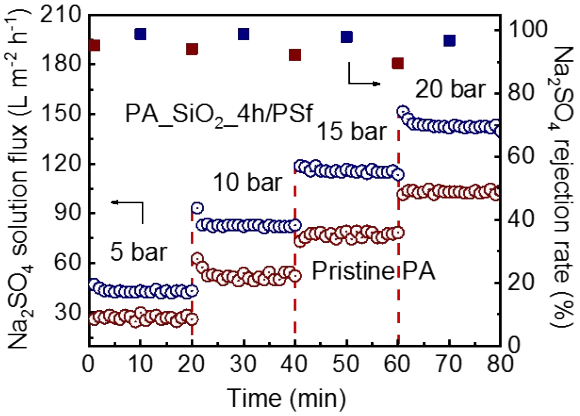

Fig. S21 Perm-selectivity of pristine PA and PA_SiO_2_4h/PSf TFC membranes toward Na_2SO_4 aqueous solution (1000 ppm) under varied transmembrane pressure (5–20 bar).

With an increase in the applied pressure, the corresponding water flux of the TFC membranes increased, and the rejection was slightly compromised (**Fig. S21**). This was because of the synergistic effects of loose intermolecular chains of soft semi-aromatic PA nanofilms and the significant ion concentration polarization (ICP) under high pressures. Notably, both pristine PA and PA_SiO_2_4h/PSf TFC membranes retained their structural integrity during the pressure cycling experiments.

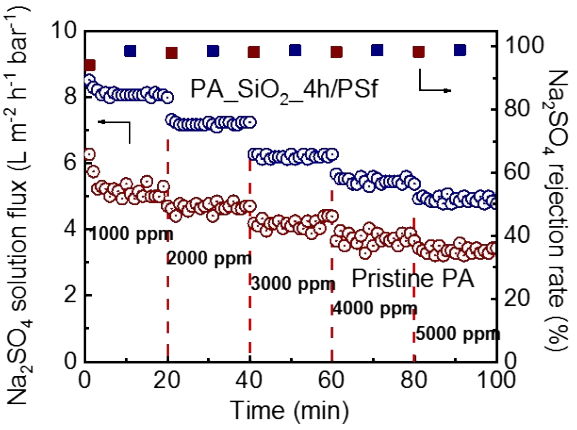

Fig. S22 Influence of Na_2SO_4 concentration on the perm-selectivity of the pristine PA and PA_SiO_2_4h/PSf TFC membranes under the filtration condition of 10 bar, at 398 K.

We explored the influence of the Na_2SO_4 concentration on the perm-selectivity of the pristine PA and PA_SiO_2_4h/PSf TFC membranes (**Fig. S22**). The water flux decreased along with the gradually enhanced salt concentration because of the enhanced osmotic pressure. The water flux of the PA_SiO_2_4h/PSf TFC membrane decreased from 8.4 $L{\cdot}m^{-2}{\cdot}h^{-1}{\cdot}bar^{-1}$ to 4.9 $L{\cdot}m^{-2}{\cdot}h^{-1}{\cdot}bar^{-1}$ under Na_2SO_4 concentrations of 1000 ppm and 5000 ppm, respectively, while the Na_2SO_4 rejection rate remained constant at approximately 98.8%. In addition, the resistance toward high-concentration salt illustrates the structural robustness of the PA_SiO_2_4h/PSf TFC membrane.

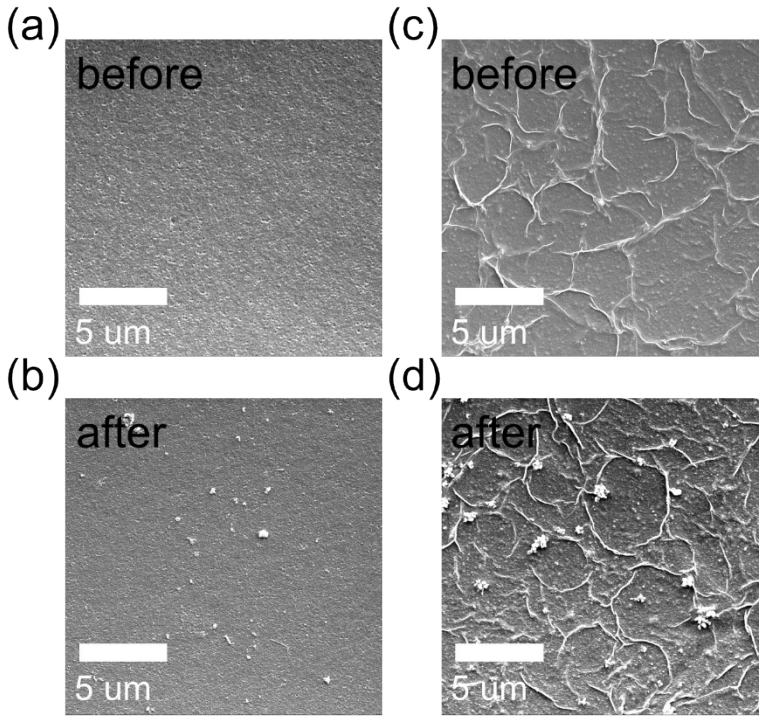

Fig. S23 FESEM images with pristine PA (left-hand panel) and PA_SiO_2_4h/PSf membranes (right-hand panel) before (a, c) and after (b, d) long-term pure water filtration.

The surface SEM images of the pristine PA and the optimum PA_SiO_2_4h/PSf membranes after their long-term pure water (1600 min) and 1000 ppm Na_2SO_4 filtration test (800 min) have been examined, and the results have been added in **Fig. S23**, which can be clearly seen that the surface microstructures were nearly remained before/after long-term filtration tests.

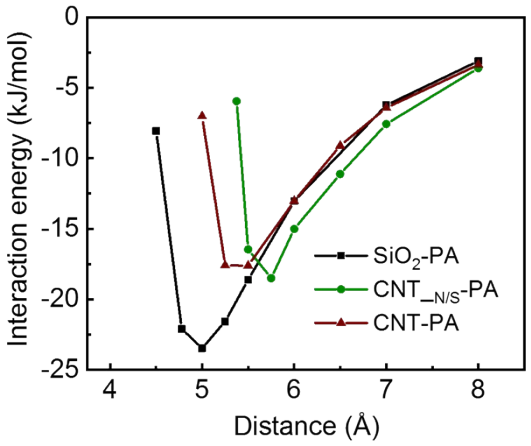

Fig. S24 The distance-dependent interaction energy of the SiO_2-PA, $CNT_{\_N/S}$-PA, and CNT-PA systems.

From the MD simulation result, we can draw such a conclusion that the SiO_2-PA has a higher interaction force than that of $CNT_{\_N/S}$-PA and CNT-PA with lower interaction energy. The minimum interaction energy of SiO_2-PA, $CNT_{\_N/S}$-PA, and CNT-PA are -23.47, -18.41, and -17.61 kJ mol^{-1} at the distance of 5 Å, 5.75 Å, and 5.5 Å, respectively. This result verifies the more intense interfacial connection between the newly-developed SiO_2 interlayer, owing to the superior hydrophilicity with large amounts of hydroxyl groups that interconnects with the active sites (carbonyl and amine groups) of PA.[9, 10]

Table S1 Surface profiles of pristine PSf and SiO_2_4h/PSf porous membranes acquired from AFM characterization over a scanning area of 10 μm × 10 μm.

Sample	RMS (nm)	Ra (nm)	Surface area (nm^2)
PSf	7.5	6.1	1.03×10^8
SiO_2_4h/PSf	37.4	25.1	1.12×10^8

Table S2 Atomic composition of porous supports calculated by XPS measurements.

Sample	C (%)	O (%)	S (%)			Si (%)		
			S 2s	S 2p3/2	S total	Si 2s (%)	Si 2p3/2 (%)	Si total
PSf	79.48	14.15	3.04	3.33	6.37	0	0	0
SiO_2_1h/PSf	77.83	14.28	2.59	3.48	6.07	0.38	1.44	1.82
SiO_2_2h/PSf	62.8	22.41	1.94	3.94	5.88	5.76	3.15	8.91
SiO_2_4h/PSf	53.64	25.60	1.12	1.98	3.10	9.84	7.82	17.66
SiO_2_6h/PSf	51.78	26.41	0.89	2.10	2.99	9.97	8.85	18.82

Table S3 Surface properties of pristine PA and PA_SiO_2/PSf TFC membranes. These results were acquired from AFM measurements over a scanning area of 20 μm × 20 μm.

Sample	Height (nm)	Surface area (nm^2)	Ra (nm)	RMS (nm)	Surface pattern width (nm)
Pristine PA	79.3	4.245×10^8	9.71	12.61	~ 80
PA_SiO_2 _1h/PSf	171.5	4.257×10^8	15.42	22.33	~ 180
PA_SiO_2 _2h/PSf	180.2	4.311×10^8	24.16	38.22	~ 200
PA_SiO_2 _4h/PSf	243.5	4.362×10^8	72.22	75.90	~ 150
PA_SiO_2 _6h/PSf	269.9	4.417×10^8	73.26	88.71	~ 200

Table S4 Summary of PIP storage capacity, PIP diffusion rate $S_{PIP\text{-}O;}$ within the first 30 s), and relative monomer diffusion rate *(D_r*; within the first 30 s) on various substrates.

Sample	Storage capacity ($g \cdot m^{-2}$)	Diffusion rate ($g \cdot L^{-1} \cdot min^{-1}$)	Relative diffusion rate (min^{-1})
Pristine PA	6.01	24.18×10^{-3}	0.201
PA_SiO_2_4h/PSf	6.26	17.54×10^{-3}	0.139
PA_SiO_2_6h/PSf	6.35	22.06×10^{-3}	0.173

Table S5 The rejections of TFC PA membranes for different neutral sugars solutes.

Samples	Glycerol	Glucose	Sucrose	Raffinose
Pristine PA	20.06	71.25	95.27	95.32
PA_SiO_2_1h/PSf	20.17	71.31	93.88	93.11
PA_SiO_2_2h/PSf	16.95	68.31	95.77	94.41
PA_SiO_2_4h/PSf	13.47	62.78	95.38	94.92
PA_SiO_2_6h/PSf	6.86	47.91	91.94	91.97

Table S6 Atomic composition and degree of crosslinking of pristine PA and PA_SiO_2/PSf membranes.

Sample	C (%)	O (%)	N (%)	O/N ratio	Degree of crosslinking (%)
Pristine PA	70.01	16.93	13.06	1.2963	61.30
PA_SiO_2 _1h/PSf	73.14	14.87	11.99	1.2401	67.86
PA_SiO_2 _2h/PSf	66.53	18.51	14.96	1.2373	68.18
PA_SiO_2 _4h/PSf	70.92	16.08	13.00	1.2369	68.23
PA_SiO_2 _6h/PSf	67.35	17.75	14.90	1.1913	73.81

Table S7 The MWCO values and the mean pore size of the as-formed PA-based membranes.

Samples	MWCO (Da)	50% rejection (Da)	84.13% rejection (Da)	d_p (nm)	d_s (nm)	σ_p
Pristine PA	304	143.4	266.5	0.3217	0.4293	1.3345
PA_SiO_2_1h/PSf	310	143.4	272.4	0.3217	0.4337	1.3482
PA_SiO_2_2h/PSf	307	148.8	272.4	0.3273	0.4337	1.3251
PA_SiO_2_4h/PSf	318	157.4	286.6	0.3360	0.4440	1.3214
PA_SiO_2_6h/PSf	334	187.8	313.2	0.3647	0.4628	1.2690

Table S8 Performance of reported state-of-the-art nanofiltration membranes.

Membrane and description	Membrane abbreviation	PWP ($L \cdot m^2 \cdot h^{-1} \cdot bar^{-1}$)	Salt rejection (%)			Cl^-/SO_4^{2-} Selectivity	References
			Na_2SO_4	$MgSO_4$	NaCl		
Commercial membranes	DOW FILMTEC™ NF70	7.2	97.0	70.0	70.0	10.0	11
	DOW FILMTEC™ NF90	6.7	98.0	90.0	90.0	5.00	
	GE-Osmonics DL	10.0	96.0	96.0	40.0	15.0	
	GE-Osmonics HL	6.9	97.0	97.0	33.0	23.3	
	Synder NFX	2.4	99.0	99.0	40.0	60.0	
	Synder NFW	5.4	97.0	97.0	20.0	26.7	
NF membranes with cellulose nanocrystals as an interlayer	PA50/CNC/PES	34	97.7	86	6.5	40.7	12
MXene Nanosheet Templated Nanofiltration Membranes	TFC_nO	45.7	96.0	94	18	20.5	13
TFC NF membranes fabricated from polymeric amine, polyethylenimine embedded with monomeric amine, And piperazine for enhanced salt separation	$PEI_{2.4}$-$PIP_{0.6}$/TMC	5.1	50.0	74	65.0	0.70	14
	$PEI_{0.6}$/TMC-$PIP_{2.4}$/TMC	1.2	68.0	94	78.0	0.69	
Enhancing the performance of polyethylenimine-modified NF membranes by coating a layer of sulfonated poly(ether ketone) for removing sulfamerazine	SPEEK/PEI-PI # 5 m	3.4	69.7	> 90	57.6	1.4	15
	SPEEK/PEI-PI # 10 m	2.9	86.6	> 90	60.8	2.9	
	SPEEK/PEI-PI # 30 m	2.3	86.6	> 90	66.9	2.5	
	SPEEK/PEI-PI # 60 m	2.0	86.6	> 90	70.4	2.2	
Polyamide nanofiltration membrane with highly uniform sub-nanometre pores for sub-1 Å precision separation	(PIP+SDS)/TMC	17.1	99.6	98.2	27.0	182	16
pH-responsive NF membranes containing carboxybetaine with tunable ion selectivity for charge-based separation	PCHM1	2.2	83.4	58	5.2	5.7	17
	PCHM2	3.8	74.4	56	4.4	3.7	
Oligo-ethylene-glycol-based thin-film composite NF membranes for effective separation of mono-/di-valent anions	PA@EDA 0.15%	4.2	98.0	-	24.8	37.6	18
	PA@EDA 1%	1.1	91.2	-	27.6	8.2	
	PA@EDA 2%	0.6	61.4	-	27.5	1.9	
	PA@DCA 0.2%	8.3	98.5	-	12.6	58.3	
	PA@DCA 1.5%	1.5	96.5	-	17.5	23.6	
	PA@DCA 2.5%	1.3	95.0	-	13.2	17.4	
Alginate Hydrogel Assisted Controllable Interfacial Polymerization for High-Performance Nanofiltration Membranes	SA-15.5	30.3	97.2	82.7	15.2	30.3	19
TiO2@graphene oxide incorporated antifouling nanofiltration membrane	NFM-3 # 0.2 wt% TiO_2 @GO	5.6	98.8	58	35	54.17	20

Ultrathin PA membrane with decreased porosity and superior antifouling properties	BTC-PIP	8.7	99.1	99.4	83.3	18.6	[21]
Nanovoid membranes embedded with hollow zwitterionic nanocapsules	TFNM with HZN_{CS}	12.2	94.7	93.4	38.2	11.7	[22]
MPD based nanofiltration membrane	NMP-act.	10.9	99.9	99.9	94.3	57	[23]
	DMF-act.	12.1	99.9	99.9	91.4	86	
	DMSO-act.	14.5	99.9	99.9	85.1	149	
Polydopamine-coated silica nanoparticles embedded thin-film nanocomposite nanofiltration membranes	$TFN_{PDA\text{-}SiNPs}$	13.3	97.0	94.0	35.0	21.7	[24]
Polyphenol intermediate layer for nanofiltration	NFM-15	23.7	99.4	99.4	33.4	114	[25]
Phosphonium modification leads to ultrapermeable antibacterial polyamide composite membranes with unreduced thickness	THPC-5	50.5	98.4	93.8	22.0	48.8	[26]
Preparation of TFC NF membranes with improved structural stability through the mediation of polydopamine	PA/PA-PES	11.4	93.5	82.4	31.0	10.6	[27]
	PA/PES	14.6	83.4	70.6	16.9	5.0	
Tuning the functional groups of carbon quantum dots in thin-film nanocomposite membranes for nanofiltration	PA-TFC	3.0	95.5	89.0	30.2	15.5	[28]
	TFN-SCQD	7.0	93.8	82.0	8.8	14.7	
	TFN-NCQD	5.2	91.7	90.0	30.5	8.4	
	TFN-CCQD	6.1	93.6	87.0	16.8	13.0	
Thin-film composite membranes with aqueous template-induced surface nanostructures for enhanced NF	TFC-R	21.3	99.4	-	43.5	94.2	[29]
	TFC-T	5.7	98.5	98.5	48.3	34.5	
SDS-intervened NF membrane	TFC-control	4.9	97.2	93.4	40.5	21.2	[30]
	TFC-SDS	7.5	92.3	93.8	47.0	6.9	
PD/SWCNTs film supported ultrathin polyamide NF membrane	PD/SWCNTs	*40.2	95.9	94.1	22.7	18.9	[31]
Sub-5 nm polyamide nanofilm	NFM #1	68.0	96	84.8	9.8	22.55	[32]
PDA inter-mediated nanofilm	PA/PD-PES	11.4	93.5	82.4	31	10.6	[33]
CNTs intermediated nanofiltration membrane	TFC-2	21	98.5	98.3	18.8	54.1	
SiO_2 inter-modulated PA-NF membrane	PA_SiO_2_4h/PSf	14.5	98.7	97.9	20.8	60.9	This work
	PA_SiO_2 _6h/PSf	20.6	94.7	91.6	13.2	16.4	
	Pristine PA	4.8	98.8	91.4	21.2	65.8	

* Water permeance of NaCl feed was considered as the pure water permeance.

References

1. Y. Lin, M. S. Salem, L. Zhang, Q. Shen, A. H. El-shazly, N. Nady and H. Matsuyama, *J. Membr. Sci.*, 2020, **606**, 118141.
2. T. Istirokhatun, Y. Lin, S. Wang, Q. Shen, J. Segawa, K. Guan and H. Matsuyama, *Chem. Eng. J.*, 2021, **417**, 127903.
3. L. Zhang, Y. Lin, H. Wu, L. Cheng, Y. Sun, T. Yasui, Z. Yang, S. Wang, T. Yoshioka and H. Matsuyama, *J. Mater. Chem. A*, 2019, **7**, 24569-24582.
4. C. C. Carcouet, M. W. van de Put, B. Mezari, P. C. Magusin, J. Laven, P. H. Bomans, H. Friedrich, A. C. Esteves, N. A. Sommerdijk, R. A. van Benthem and G. de With, *Nano Lett.*, 2014, **14**, 1433-1438.
5. S. Yuan, G. Zhang, J. Zhu, N. Mamrol, S. Liu, Z. Mai, P. Van Puyvelde and B. Van der Bruggen, *J. Mater. Chem. A*, 2020, **8**, 3238-3245.
6. C. Jiang, L. Zhang, P. Li, H. Sun, Y. Hou and Q. J. Niu, *ACS Appl. Mater. Interfaces*, 2020, **12**, 25304-25315.
7. B. Yuan, S. Zhao, P. Hu, J. Cui and Q. J. Niu, *Nat. Commun.*, 2020, **11**, 1-12.
8. Y. Zhu, P. Dou, H. He, H. Lan, S. Xu, Y. Zhang, T. He and J. Niu, *Sep. Purif. Technol.*, 2020, **239**, 116528.
9. M. Wang, W. Dong, Y. Guo, Z. Zhai, Z. Feng, Y. Hou, P. Li and Q. J. Niu, *Desalination*, 2021, **513**, 114836.
10. Y. Gong, S. Gao, Y. Tian, Y. Zhu, W. Fang, Z. Wang and J. Jin, *J. Membr. Sci.*, 2020, **600**, 117874.
11. Y.-J. Tang, Z.-L. Xu, S.-M. Xue, Y.-M. Wei and H. Yang, *J. Membr. Sci.*, 2016, **498**, 374-384.
12. J.-J. Wang, H.-C. Yang, M.-B. Wu, X. Zhang and Z.-K. Xu, *J. Mater. Chem. A*, 2017, **5**, 16289-16295.
13. D. Xu, X. Zhu, X. Luo, Y. Guo, Y. Liu, L. Yang, X. Tang, G. Li and H. Liang, *Environ. Sci. Technol.*, 2021, **55**, 1270-1278.
14. D. Wu, S. Yu, D. Lawless and X. Feng, *React. Funct. Polym.*, 2015, **86**, 168-183.
15. S. Zhao, Y. Yao, C. Ba, W. Zheng, J. Economy and P. Wang, *J. Membr. Sci.*, 2015, **492**, 620-629.
16. Y. Liang, Y. Zhu, C. Liu, K. R. Lee, W. S. Hung, Z. Wang, Y. Li, M. Elimelech, J. Jin and S. Lin, *Nat. Commun.*, 2020, **11**, 1-9.
17. X.-D. Weng, X.-J. Bao, H.-D. Jiang, L. Chen, Y.-L. Ji, Q.-F. An and C.-J. Gao, *J. Membr. Sci.*, 2016, **520**, 294-302.
18. D. Ren, X.-T. Bi, T.-Y. Liu and X. Wang, *J. Mater. Chem. A*, 2019, **7**, 1849-1860.
19. Z.-Y. Ma, Y.-R. Xue and Z.-K. Xu, *Membranes*, 2021, **11**, 1-11.
20. J. Wang, Y. Wang, J. Zhu, Y. Zhang, J. Liu and B. Van der Bruggen, *J. Membr. Sci.*, 2017, **533**, 279-288.
21. B. Yuan, C. Jiang, P. Li, H. Sun, P. Li, T. Yuan, H. Sun and Q. J. Niu, *ACS Appl. Mater. Interfaces*, 2018, **10**, 43057-43067.
22. Z. Sun, Q. Wu, C. Ye, W. Wang, L. Zheng, F. Dong, Z. Yi, L. Xue and C. Gao, *Nano Lett.*, 2019, **19**, 2953-2959.
23. M. G. Shin, S. J. Kwon, H. Park, Y.-I. Park and J.-H. Lee, *J. Membr. Sci.*, 2020, **595**, 117590.
24. M. B. M. Y. Ang, C. A. Trilles, M. R. De Guzman, J. M. Pereira, R. R. Aquino, S.-H. Huang, C.-C. Hu, K.-R. Lee and J.-Y. Lai, *Sep. Purif. Technol.*, 2019, **224**, 113-120.
25. H. Sun, J. Liu, X. Luo, Y. Chen, C. Jiang, Z. Zhai and Q. J. Niu, *Desalination*, 2020, **488**, 114525.
26. H. Peng, W. H. Zhang, W. S. Hung, N. Wang, J. Sun, K. R. Lee, Q. F. An, C. M. Liu and Q. Zhao,

Adv. Mater., 2020, **32**, e2001383.

27. Y. Li, Y. Su, J. Li, X. Zhao, R. Zhang, X. Fan, J. Zhu, Y. Ma, Y. Liu and Z. Jiang, *J. Membr. Sci.*, 2015, **476**, 10-19.
28. M. Wu, J. Yuan, H. Wu, Y. Su, H. Yang, X. You, R. Zhang, X. He, N. A. Khan, R. Kasher and Z. Jiang, *J. Membr. Sci.*, 2019, **576**, 131-141.
29. C. Wei, Z. He, L. Lin, Q. Cheng, K. Huang, S. Ma and L. Chen, *J. Membr. Sci.*, 2018, **563**, 752-761.
30. H. Sun and P. Wu, *J. Membr. Sci.*, 2018, **564**, 394-403.
31. Y. Zhu, W. Xie, S. Gao, F. Zhang, W. Zhang, Z. Liu and J. Jin, *Small*, 2016, **12**, 5034-5041.
32. S. Pulak, M. Solagna, R. Santanu, A. Vasista, K. A. Reddy and S. Karan, *J. Mater. Chem. A*, 2021, **9**, 20714-20724.
33. C. Ji, Z. Zhai, C. Jiang, P. Hu, S. Zhao, S. Xue, Z. Yang, T. He and Q. J. Niu, *Desalination*, 2021, **500**, 114869.